

Centrifugal instability of Stokes layers in crossflow: the case of a forced cylinder wake

JUAN D'ADAMO¹, RAMIRO GODOY-DIANA² & JOSÉ EDUARDO WESFREID²

¹Facultad de Ingeniería Universidad de Buenos Aires (CONICET), Av. Paseo Colón 850,
C1063ACV - Buenos Aires - Argentina.

²Physique et Mécanique des Milieux Hétérogènes (PMMH), CNRS UMR 7636; ESPCI
ParisTech; UPMC; Univ. Paris Diderot (Paris 7), 10 rue Vauquelin, 75005 Paris, France

Abstract

The wake flow around a circular cylinder at $Re \approx 100$ performing rotatory oscillations has been thoroughly discussed in the literature, mostly focusing on the modifications to the natural Bénard-von Kármán vortex street that result from the forced shedding modes locked to the rotatory oscillation frequency. The usual experimental and theoretical frameworks at these Reynolds numbers are quasi-two-dimensional, since the secondary instabilities bringing a three-dimensional structure to the cylinder wake flow occur only at higher Reynolds numbers. In the present paper we show that a three-dimensional structure can appear below the usual three-dimensionalization threshold, when forcing with frequencies lower than the natural vortex shedding frequency, at high amplitudes, as a result of a previously unreported mechanism: a pulsed centrifugal instability of the oscillating Stokes layer at the wall of the cylinder. The present numerical investigation lets us in this way propose a physical explanation for the turbulence-like features reported in the recent experimental study of D'Adamo et al. (2011).

1 Introduction

A circular cylinder performing rotational oscillations around its axis in an infinite viscous fluid produces an axisymmetric pulsed boundary layer, called a Stokes layer. This is a flow susceptible to generate centrifugal instabilities. The linear stability problem of this flow configuration has been studied by Hall (1975); Seminara and Hall (1976) using asymptotic methods. A threshold for the appearance of three-dimensional (3D) axisymmetric instability modes was determined. Riley and Laurence (1976) did also stability calculations not directly on the Stokes layer problem but considering the modulated circular Couette flow under axisymmetric disturbances, in the narrow-gap limit. Later, Aouïdef et al. (1994); Ern (1998); Ern and Wesfreid (1999, 2002) considered this flow as a limit case for the stability problem of the classic geometry of two concentric cylinders with oscillation: the Taylor-Couette configuration (see e.g. Chandrasekhar (1981) for a review). In both cases, the control parameter is the Taylor number, defined as

$$T = R_i \sqrt{\frac{d}{\mathcal{R}}} \quad (1)$$

where $R_i = \omega_i r_i d / \nu$ is a Reynolds number based on the rotational angular velocity of the cylinder ω_i . We keep the notation of the Taylor-Couette configuration, where the subscript i stands for

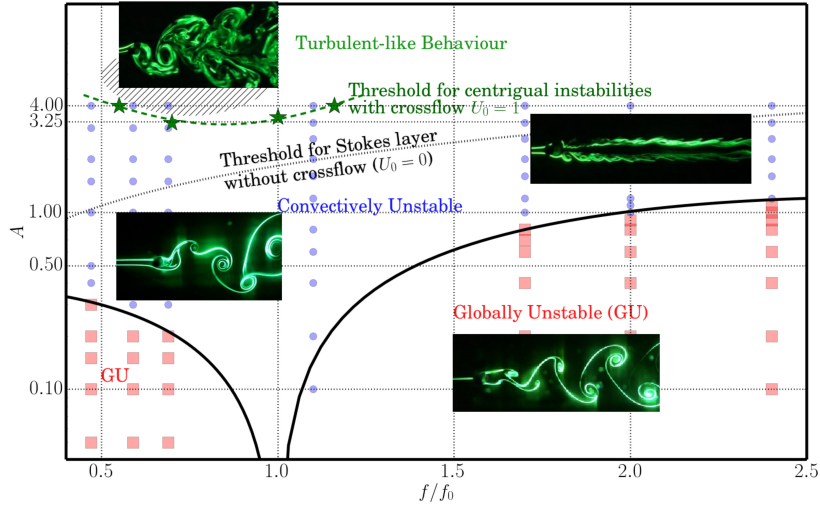


Figure 1: Different flow states for the forcing parameters (f, A) scrutinised in D’Adamo et al. (2011). Visualisations are from Thiria et al. (2006). Solid lines represent the threshold from global to convective instability. The dotted line indicates the threshold to centrifugal instability of the Stokes layer of an oscillating cylinder without a crossflow given by $T_c = 165$, from Seminara and Hall (1976). Symbols ★ show the threshold for 3D centrifugal instabilities observed in the 3D DNS discussed in Figs. 5(b) and 5(c). Dashed region stands for states with turbulent-like behaviour described in D’Adamo et al. (2011).

inner cylinder, r_i thus being the radius of the cylinder. In addition, \mathcal{R} is the local radius of curvature and ν the kinematic viscosity. The characteristic length scale d in the Taylor-Couette case is the gap between the cylinders, which fixes the scale of the wavelength of the primary instability. For the case studied by Seminara and Hall (1976), however, the instability occurs in the inner Stokes boundary layer of thickness $\delta_S = \sqrt{\nu/\omega_i}$ around the oscillating cylinder. They have determined analytically, numerically and experimentally the critical values for T associated with the onset of a Taylor-Couette-type vortex flow. Vortices evenly spaced, with a critical length λ_c in the cylinder axial direction which is proportional to δ_S , are thus developed.

On the other hand, when a uniform flow comes across a cylinder, a prototypical 2D wake flow takes place for moderate free-stream Reynolds numbers $Re = DU_0/\nu$, where D is the diameter of the cylinder, U_0 the free-stream velocity. The well-known Bénard-von Kármán (BvK) vortex street (Bénard, 1908; von Kármán, 1911) results from the destabilisation of the steady flow in the wake of the cylinder and produces the periodic shedding of opposite-signed vortices with a frequency f_0 , that occurs above the threshold $Re_c \approx 47$ (see e.g. Provansal et al. (1987); Jackson (1987)). This flow is quasi-two dimensional up to $Re \lesssim 180$. In a recent work (D’Adamo et al., 2011), we studied experimentally the problem of the forced wake performing rotary oscillations at $Re = 100$. The rotational oscillation of the cylinder is prescribed by a forcing function of frequency f and amplitude θ_0 that can be written as $\theta(t) = \theta_0 \cos(2\pi ft)$, which allows the forcing to be unequivocally described using two independent non-dimensional parameters as did by Taneda (1978): the forcing amplitude $A = u_{\theta\max}/U_0$, where $u_{\theta\max} = D\pi f\theta_0$ is the maximal azimuthal velocity of the rotational oscillation, and the ratio f/f_0 . We characterised the spatial development of the flow and its stability properties following previous studies by Thiria et al.

(2006); Thiria and Wesfreid (2007). A synthesis of the case study is presented in Figure 1. From the analysis of power density spectra of the flow we gave a detailed description of the forced wake, giving insight on the energy distribution, the different frequency components, and in particular on a continuous spectrum observed for a high amplitude of the forcing oscillation. Furthermore, vortex structures revealed turbulence-like features like splitting and mixing in a spatial cascade pattern. A question remained concerning the physical mechanism present in the bifurcation that triggers such behaviour of the wake.

We speculated on a 3D centrifugal instability to be at the origin of this sequence of transitions. A natural first attempt to test this idea is shown in figure 1, where the critical Taylor number $T_c = 165$ corresponding to the instability threshold of the pure rotatory oscillating cylinder case without crossflow studied by Seminara and Hall (1976) is identified in the frequency-amplitude phase space (f, A) of the forced wake of D’Adamo et al. (2011). This crude estimate for a threshold is compatible with the experimental points where the turbulent-like behaviour was observed (low frequencies and high amplitudes of the forcing oscillation). The purpose of the present paper is to characterize in detail the existence of a 3D instability and its centrifugal nature, using analytical estimations from the 2D flow and from 3D direct numerical simulations (DNS).

It is worth mentioning that centrifugal instabilities were also reported for forced flows with different configurations. For transverse oscillations of a cylinder in a fluid at rest, Honji (1981), obtained visualizations that identified 3D structures produced by centrifugal instabilities. Hall (1984) performed a stability analysis of this configuration and gave a theoretical explanation. Tatsuno and Bearman (1990) investigated in detail the patterns and the structure of the flows that result from these instabilities. Later, Elston et al. (2004) addressed DNS calculations and Floquet stability analysis for this problem.

Three dimensional instabilities in wake flows have been studied theoretically and numerically by Blackburn et al. (2005) where it was determined that bifurcations to three-dimensionality can occur from a two-dimensional time-periodic base state with space–time reflection symmetry for the wake of symmetrical bluff bodies. More recently for the case of the two-dimensional stationary flow past a rotating cylinder, Pralits et al. (2013) suggest that the stationary unstable three-dimensional mode could be the result of a hyperbolic instability.

Lo Jacono et al. (2010) were interested on the role of rotationally oscillations can modify the three-dimensional transition in the wake of a cylinder. The frequency of oscillation was matched to the natural vortex-shedding frequency, $f^+ = 1$, for $Re = 300$. They reported changes on the three dimensional modes from Floquet stability analysis on two-dimensional periodic flow. They found that the rotational oscillation dramatically suppressed mode B, even for small amplitudes of oscillation. Mode A was also damped, but not as significantly as mode B. For what they considered high rotational oscillation amplitudes, in our notation $A \simeq 0.66$ they identify a new three-dimensional transition mode, which they called D mode, that shares the same symmetries as mode A.

Three dimensional characteristics of forced wakes have been recently studied by Kumar et al. (2013) for the case of rotational oscillations at $Re = 185$ near the transition, using flow visualization, hot-wire anemometry and PIV. Spatial distribution of lock-on regions and its relationship with the forcing frequencies and amplitudes were determined. They also found that for certain forcing parameters (f^+, A) , the flow can be forced to become two-dimensional. Studied amplitudes were up to $A = \pi$, a value below the threshold found in D’Adamo et al. (2011) by means of spatio-temporal spectral analysis.

To summarise, the present work sets up a new view about 3D instabilities in wake flows, which have often been discussed in the case of the circular cylinder for $Re > 180$ as secondary instabilities to the BvK vortex street. We organise the paper as follows: in the next section we

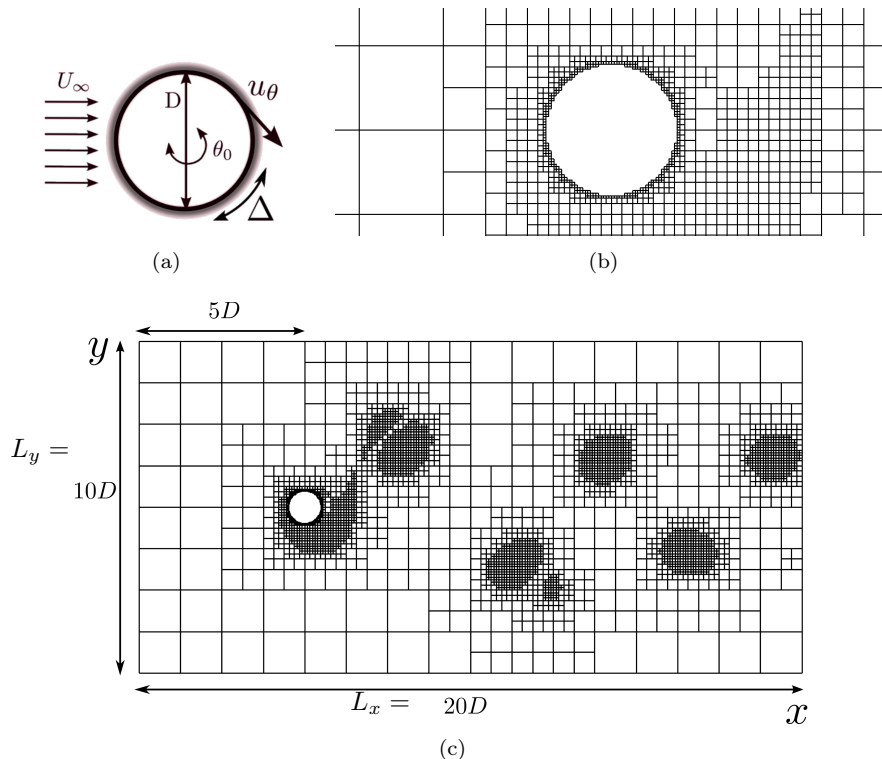


Figure 2: a) Parameters of the problem. b) The adaptive 2D mesh around the circular cylinder shows the octree structure. c) Problem domain.

describe the method used for the direct numerical simulations (DNS); results are presented in Section 3 where we determine the 3D stability threshold; in Section 4 we investigate the instability nature, using some concepts of centrifugal instabilities and propose therefore a reduction of the complex problem; lastly we elaborate our conclusions in Section 5, showing analogies with the Taylor-Couette problem of eccentric cylinders.

2 Problem definition for DNS

In order to study this problem, we performed 2D and 3D direct numerical simulations with Gerris free software, a parallelised tree-based adaptive solver for Navier-Stokes equations Popinet (2003). The code combines an adaptive multi-grid finite volume method and the methods of immersed boundary and volume of fluid (VOF). The basic equations are the incompressible continuity equation and Navier-Stokes equations, which can be written in terms of the velocity $\mathbf{u} = (u, v, w)$ and pressure p fields as:

$$\frac{\partial \mathbf{u}}{\partial t} + (\mathbf{u} \cdot \nabla) \mathbf{u} = -\frac{\nabla p}{\rho} + \nu \nabla^2 \mathbf{u} \quad \nabla \cdot \mathbf{u} = 0 \quad (2)$$

The domain is spatially discretised using cubic finite volumes organised hierarchically as an octree. Along with the forcing problem parameters, a 2D example of the spatial discretisation

is given in Figure 2. The flow domain, shown in Figure 2(c) is $L_x \times L_y = 20D \times 10D$ for 2D simulations and $L_z = 20D$ for the spanwise direction in 3D simulations. As detailed in Popinet (2003) the mesh can be refined near the solid boundary and it can use vorticity gradients as an adaptive criterion. A cell is refined whenever:

$$\frac{|\nabla \times \mathbf{u}| \Delta x}{\max |\mathbf{u}|} > \xi \quad (3)$$

where Δx is the size of the cell and ξ is a user-defined threshold which can be interpreted as the maximum angular deviation (caused by the local vorticity) of a particle travelling at speed $\max |\mathbf{u}|$. This adaptive criterion is represented in Figure 2(b) and 2(c) where different box sizes are noticeable. In order to reveal BvK vortices as well as centrifugal structures, we choose a minimum grid size of $D/51.2$ for the solid boundary and $D/12.8$ to define vortex regions. The ξ threshold is set to 0.05 for 3D simulations and to 0.01 for 2D simulations. The flow parameters of the simulations are defined in order to match the experimental case of D’Adamo et al. (2011): Cross flow velocity $U_\infty = 1$, kinematic viscosity $\nu = 10^{-3}$ and cylinder diameter $D = 0.1$, giving a Reynolds number $Re = 100$.

The boundary conditions are: $u = 1$ for $x = -5D$; $u = 1$ for $y = \pm 5$; the outflow condition is $\partial v / \partial x = 0$ and $p = 0$ for $x = 15D$; for 3D simulations, a symmetry condition is used for the flow at $z = 20D$; and at the cylinder surface, $\mathbf{u} = \mathbf{u}_{solid}$ where \mathbf{u}_{solid} depends on the forcing. As depicted in Figure 2(a) rotatory oscillations are characterised by an angular coordinate $\theta(t) = \theta_0 \cos(\alpha)$, where the forcing phase is $\alpha = 2\pi f_f t$, and tangential displacements $\Delta = u_\theta / (2\pi f_f)$. Given f_0 the natural frequency of vortex shedding, the forcing frequency f_f is written in dimensionless form as $f^+ = f_f / f_0$. A non-dimensional number for the amplitude of oscillations is obtained by comparing the maximum tangential velocity $u_{\theta max}$ and the free flow velocity, $A = u_{\theta max} / U_\infty$.

3 Results of the numerical simulation

We first performed 3D DNS numerical simulations. Figure 3 shows a case with the forcing parameters ($f^+ = 0.75$, $A = 4.00$). The isosurface of vorticity modulus in Figure 3(a) shows on one side the classic BvK wake structure synchronised with the forcing frequency. Additionally, a previously not reported effect is also clear: the modulation of the vorticity field along the direction of the cylinder axis. The two effects are depicted in Figure 3(b), revealing the 3D vortex structure around the cylinder and a well-defined wavelength λ_z . Moreover, Figure 4 shows the spatial distribution of ω_x along with ω_z for $f^+ = 0.75$, $A = 4.00$, which allows us to consider the symmetry properties of the observed mode. The spatio-temporal symmetry, H , of the two-dimensional flow is defined as:

$$H\omega(x, t) = K_y\omega(x, t + T/2) = (-\omega_x, \omega_y, -\omega_z)(x, -y, t + T/2) \quad (4)$$

where K_y is a spatial reflection. For an H -symmetric flow, from 4, the x -vorticity changes sign with $t \rightarrow t + T/2$ and $y \rightarrow -y$ at any fixed (x, z) . This is the case for mode A, whereas for mode B, the sign of x -vorticity does not change.

As studied by Blackburn et al. (2005), there are exactly three codimension-one bifurcations from a two-dimensional time-periodic base state to three-dimensional flow that are observable with variations in a single parameter. In this regard, Lo Jacono et al. (2010) showed that oscillatory forcing at $Re = 300$ leads to the appearance of a different mode (mode D) which has the same symmetries of mode A. Considering the symmetries observed in the present case

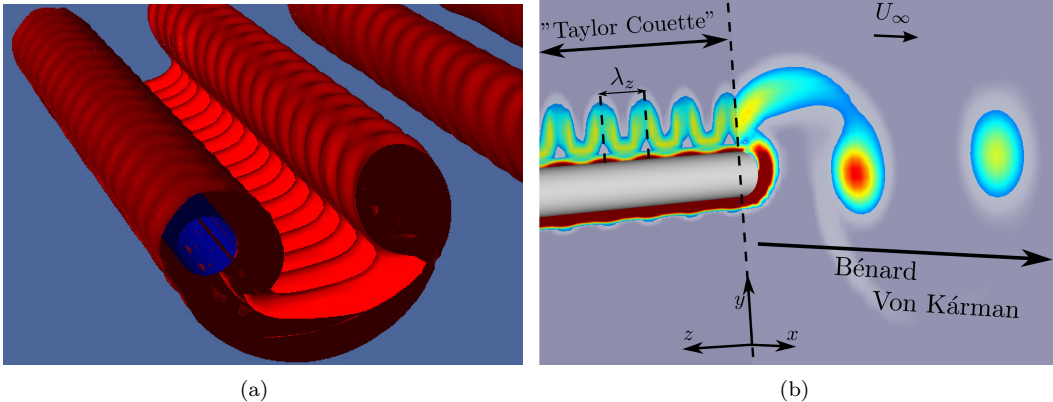


Figure 3: a) Isosurface for total vorticity modulus $\|\bar{\omega}\|$ for $f^+ = 0.75$, $A = 4.00$. b) Vorticity modulus contours for two cutting planes revealing the main flow structures ($f^+ = 0.75$, $A = 4.00$).

(Figure 4), the identified structures are not H -invariant, and they share the same symmetry as mode B.

In what follows we thoroughly scrutinise the onset of this 3D pulsed instability. Figure 5(a) shows instantaneous contours of the span-wise velocity w for a plane at $y = D/2$, revealing Taylor-Couette like vortices, with a wavelength λ_z that does not change with respect to the forcing amplitude within the range $3 < A < 4$. We can describe the flow with a Taylor number based on equation (1) considering λ_z as a characteristic length scale and $\omega_i r_i = AU_\infty$. We compute the intensity of the velocity fluctuations as $w_{rms}^2 = \int_0^{T_f} (w - \bar{w})^2 dt / T_f$, where \bar{w} is the time average of w and T_f the forcing period $T_f = 1/f^+$. The result allows us to identify a maximum value that characterises the intensity of the 3D structure for the forcing case considered.

An additional characterisation is possible by studying the amplitude of this fluctuations as a function of the forcing parameters (f^+ , A). We use the 3D DNS to study the flow modifications for two fixed forcing frequencies $f^+ = 0.75$ and $f^+ = 1.00$. A useful criterion to quantify the intensity of 3D structures is to follow the evolution of w . Given that the 3D structures are present for $A = 4.00$ (case depicted on Figure 3), we decrease the forcing amplitude from this value until they vanish. In Figure 5(b), the maxima of w_{rms} , w_{max} , are plotted against the Taylor numbers resulting from equation (1), where the characteristic length scale λ_z is found to be $1.16D$, and the corresponding forcing amplitudes. We can appreciate, looking at the square of the forcing amplitudes, that the 3D structures become damped linearly as we approach a threshold at $T = 202$ for $f^+ = 0.75$ and $T = 147$ for $f^+ = 1$. The behaviour is common to supercritical bifurcations.

Another scenario shows up when we follow the evolution of the intensity of 3D structures for a fixed forcing amplitude. There is a range of frequencies for which the instability develops. This is shown in Figure 5(c) where w_{rms}^2 is observed for $A = 4.00$ and the forcing frequency varying in a range $0.50 < f^+ < 1.20$. We can appreciate that for $f^+ \rightarrow 1.20$, w_{max}^2 decreases linearly. On the other hand, for lower frequencies, we observe that the 3D instability appears, with a finite value, for w_{max} , at $f^+ \geq 0.55$.

We perform simulations for different forcing frequencies at a fixed forcing amplitude $A = 4.00$ in order to characterise the evolution of the wavelength λ_z . We observe in Figure 6(a) that λ_z

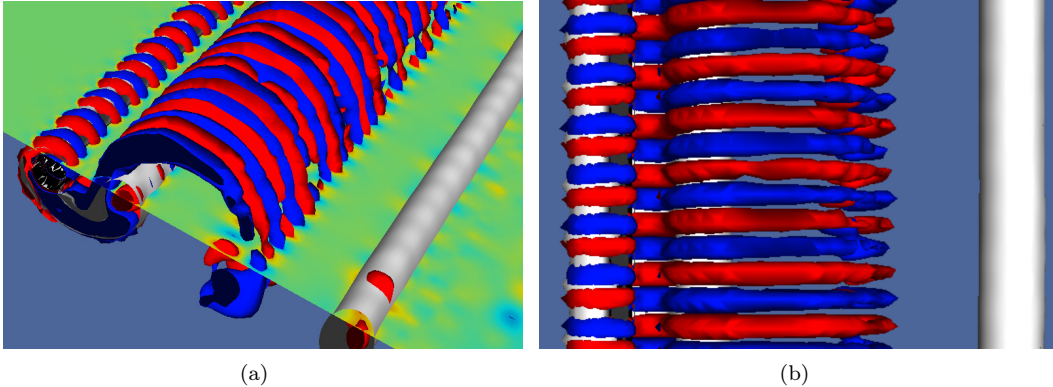


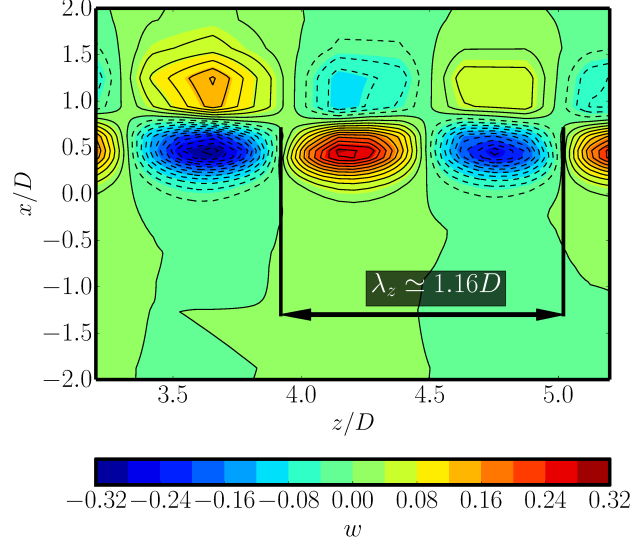
Figure 4: For forcing parameters $f^+ = 0.75$, $A = 4.00$. a) Isosurfaces for streamwise vorticity ω_x : $\omega_x = 3$ (red), $\omega_x = -3$ (blue). The white isosurface represents spanwise vorticity $\omega_z = 15$ b) Top view for isosurfaces for streamwise and spanwise vorticity.

depends on f^+ following a law $\propto (f^+)^{-1/2}$. If we assume that the “gap” size d is proportional to λ_z , from the Taylor number definition in equation (1), where T depends on $d^{3/2}$, then we expect that high forcing frequencies produce decreasing Taylor numbers. This could explain the damping of 3D fluctuations for higher frequencies in Figure 5(c). In addition, we observe that the wavelength λ_z is practically invariant with respect to the amplitude for a given frequency.

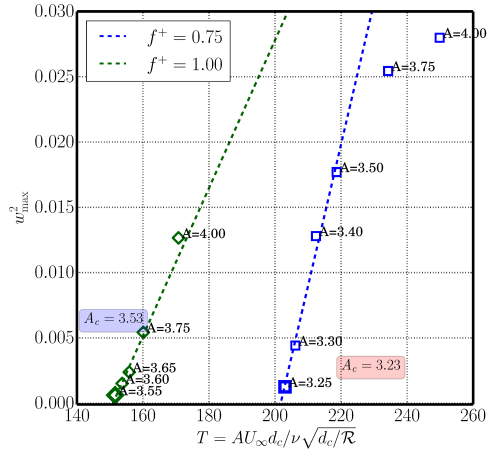
In studies of pulsed centrifugal instabilities, Riley and Laurence (1976); Carmi and Tustaniwskyj (1981); Aouidef et al. (1994) classified flow regimes based on a parameter $\gamma = \sqrt{\omega d_c^2 / 2\nu}$ which is the ratio of a centrifugal region length d_c to the Stokes layer thickness. In our experiment, γ is limited to a range between 2 and 5, it does not depend on the forcing frequency and $d_c \sim \lambda$ behaves with respect to f^+ as described in Figure 6(a), where λ decreases almost linearly as $(f^+)^{-1/2}$.

Even though the threshold for centrifugal instabilities determined in the Taylor-Couette pulsed flow is not directly applicable for a configuration with crossflow, the transformation of Taylor numbers based on the characteristic length d_c allows an approach for our results. This case presents similarity with the eccentric Taylor-Couette instability problem (see e.g. Leclercq et al. (2013); Shu et al. (2004); Siong (2006) and references therein). Indeed, in those problems, the axial wavelength of the critical perturbations is always of the same order of magnitude of the gap.

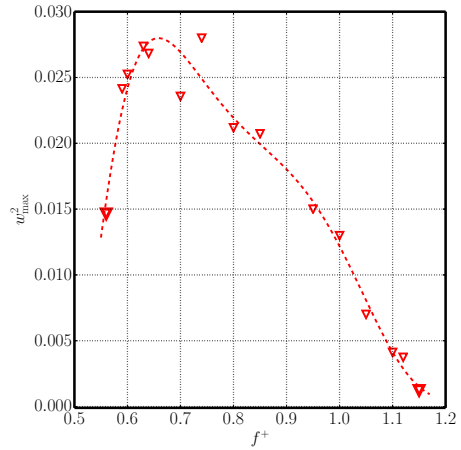
Figure 6(b) summarises the stability curves (γ, T) for centrifugal pulsed flow determined by Aouidef et al. (1994); Seminara and Hall (1976) together with the values issued from our 3D simulations. Two analytical curves show the solution corresponding to low values of γ , $T_c = 193.23\gamma^{-1}$ and high values of γ , $T_c = 15.28\gamma^{3/2}$. The curves are supported with experimental data from Aouidef et al. (1994). On the other hand, within these reference threshold frame, we plotted from our results T against γ for a fixed forcing amplitude $A = 4.00$, and for fixed forcing frequencies $f^+ = 0.75$ and $f^+ = 1.00$ (the same data used to construct Figure 5). We observe that the points are contained in the unstable region defined by the analytical curves. For $A = 4.00$, the instability develops for $0.55 < f^+ < 1.16$. When $f^+ = 1.16$, the critical point ($\gamma = 3.06$, $T = 152$) is in very good agreement with the experimental results from pure pulsed flows. For decreasing frequencies, T increases almost linearly regarding the estimated γ until for $f^+ = 0.55$ the flow stabilises with respect to centrifugal disturbances ($\gamma = 4.4$, $T = 433$). For a



(a)



(b)



(c)

Figure 5: a) Contours of the transverse component of the velocity w at a cut plane $y = D/2$. Solid and dashed lines correspond to positive and negative contour values respectively. b) Maxima of w_{rms} for a fixed forcing frequency $f^+ = 0.75$ as a function of T resulting from varying forcing amplitudes. c) Maxima of w_{rms} for a constant forcing amplitude $A = 4.00$ as a function of the forcing frequency f^+ .

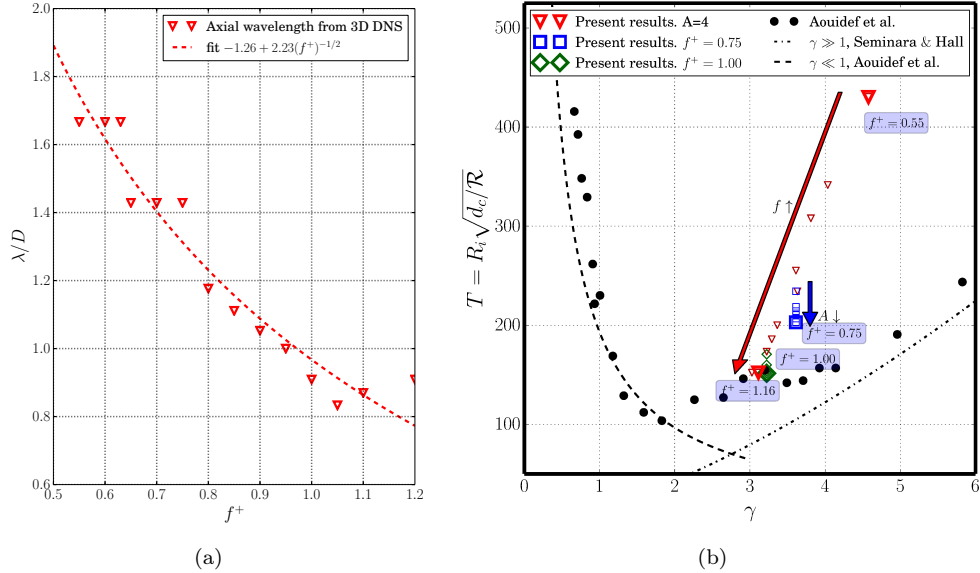


Figure 6: a) For a fixed forcing amplitude $A = 4.00$, corresponding wavelength measured in 3D simulations. b) Taylor number versus γ estimated from 3D simulations. Plotted values correspond to a fixed forcing amplitude $A = 4.00$ and to fixed forcing frequencies $f^+ = 0.75$ and $f^+ = 1.00$. Threshold points are marked in thicker symbols. The arrows represent the evolution to threshold from Fig. 5(b) and Fig. 5(c). Our results are compared with experimental and theoretical data that define instability threshold in *pure* pulsed flows from Aouïdef et al. (1994) and Seminara and Hall (1976)

fixed frequency $f^+ = 0.75$, $\gamma = 3.61$, the flow destabilises at $T = 202$ and with increasing forcing amplitudes, T eventually reaches the previous set of points at $A = 4.00$. The same behaviour is found for the fixed forcing frequency $f^+ = 1.00$, where the flow is unstable from $T = 147$.

We suggest that the centrifugal instability that develops in the forced wake can be thus considered in the context of pure rotatory pulsed oscillations. Nevertheless, the natural BvK dynamics plays an important role as the first bifurcation depends on the distance of the forcing state space parameters (f, A , Figure 1) to the resonance centred at $(f^+ = 1.00, A = 0.00)$. This fact could explain that at $f^+ < 0.55$ the centrifugal instability is not strong enough even when T is high. Conversely, for $(f^+ = 1.16, A = 4.00)$ the length d_c is significantly smaller and T decreases to the values predicted by the *pure* pulsed flow threshold.

We bring a quantitative picture of these ideas in the remainder of the paper, starting with a brief review of the criterion for centrifugal instability.

4 Centrifugal instability

The necessary condition for a 3D centrifugal instability in flows with curved streamlines is given by Rayleigh (1916) criterion for inviscid flow (see e.g Drazin and Reid, 1981) which can be

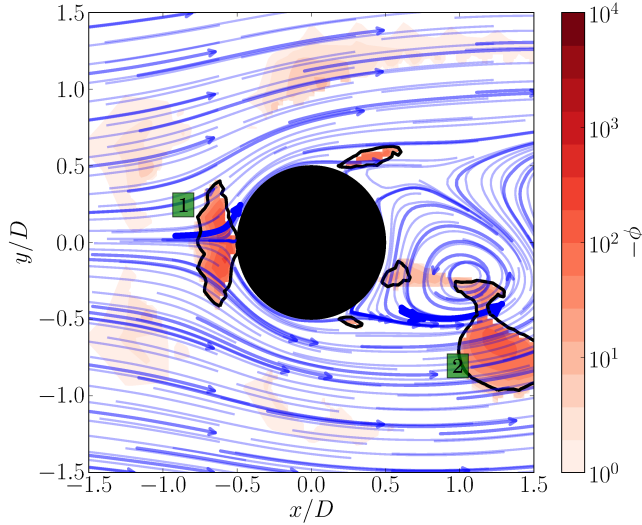


Figure 7: In non-forced wake, instantaneous streamlines and ϕ negative contours reveal potentially centrifugal instabilities regions. Regarding curvature and velocity modulus, two distinct regions associated with Görtler [1] and Taylor-Couette [2] mechanisms are marked. However, $-\phi$ is not strong enough to overcome the stabilising effect of the viscosity and to produce 3D instabilities for $Re = 100$.

written for flows such as the Taylor-Couette flow in terms of the Rayleigh discriminant

$$\phi(r) = \frac{2V}{r} \left(\frac{V}{r} + \frac{dV}{dr} \right), \quad (5)$$

where $V(r)$ is the 2D velocity of an orthoradial base flow field. 3D perturbations to this flow field are amplified if $\phi(r) < 0$, which translates the fact that the perturbed pressure field does not balance the centrifugal force, leading to flow instability. For a general profile $V(r)$, the flow field can be subdivided in regions of different stability depending on the sign of $\phi(r)$: it will be unstable in the region where $\phi(r) < 0$ and stable when $\phi(r) > 0$. More generally, for other geometries described by a vorticity field ω_z , the Rayleigh discriminant can be written as $\phi = V(r)\omega_z(r)/\mathcal{R}$ (Leblanc and Cambon, 1998; Sipp and Jacquin, 2000), where the local radius of curvature of the streamlines \mathcal{R} is defined by

$$\mathcal{R} = \frac{U^2}{(\Delta\psi)(u\nabla u)}. \quad (6)$$

Beaudoin et al. (2004) made use of these expressions in order to identify potential instability regions in a backward-facing step flow and characterise the 3D global instability. In the present case, we will see that the study of the local Rayleigh discriminant is a useful tool to predict the centrifugal stability of the forced cylinder wake problem, which lacks of symmetry simplifications. In Figure 7 the instantaneous flow streamlines along with the Rayleigh discriminant $\phi(x, y)$ are represented for a non-forced flow around a cylinder at $Re = 100$, where the flow produces the Bénard-von Kármán vortex shedding. Two distinct regions of potential centrifugal instability

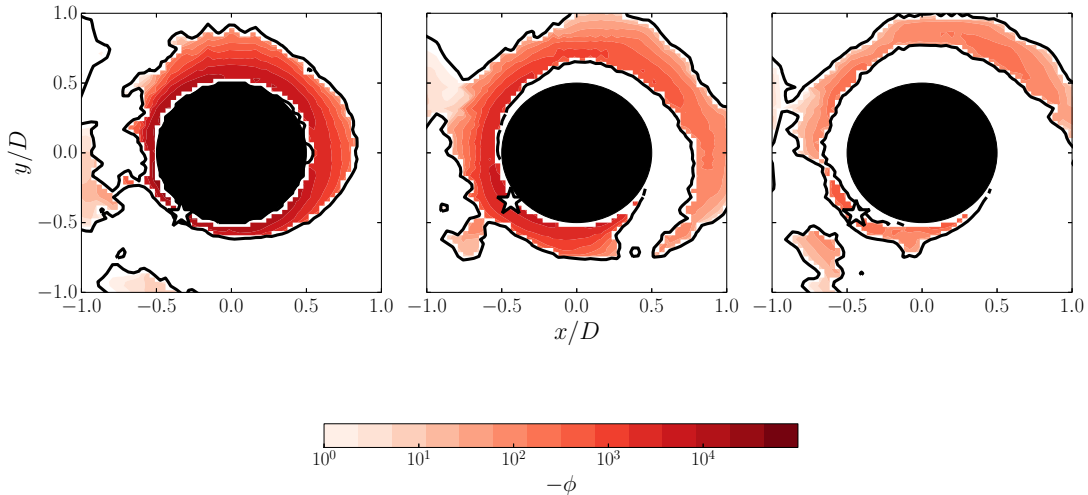


Figure 8: Rayleigh discriminant negative values contours, $\phi < 0$ for $f^+ = 0.75$ and $A = 4.00$, for three different times or oscillation phases within half of the forcing period T_f . The left picture shows ϕ spatial distribution when a vortex is shed below $x = 0$ axis, when the forcing phase $\alpha \simeq 1$. Middle ($\alpha \simeq 2$) and right ($\alpha \simeq 3$) pictures allow to appreciate the temporal and spatial evolution of ϕ . Symbol \star stands for the position \bar{x}_{\max} of $|\phi|_{\max}$.

exist: one near the stagnation point, where a concave streamline constitutes a Görtler-like geometry (Saric, 1994); and another one in the near wake side, where the curvature of the streamlines around the vortex formation region corresponds to a Taylor-Couette geometry. At $Re = 100$, nevertheless, viscosity prevents the development of 3D instabilities, which never appear for the case shown in Figure 7. When the rotational oscillatory forcing is applied, negative values of ϕ appear mostly in regions close to the cylinder. In what follows we define the characteristic length scale d_c of regions potentially unstable giving a local Rayleigh criterion to analyse the stability properties of the forced wake¹.

Despite the flow complexity, it is possible to reduce the problem to investigate solely the centrifugal instability of the 2D base flow and its relationship with the forcing parameters. We calculate the Rayleigh discriminant $\phi(\bar{x}, t)$ for each forcing parameter from the streamlines of the flow at $Re = 100$. In Figure 8, we present three snapshots of $\phi(\bar{x}, \alpha)$ at $f^+ = 0.75$, $A = 4.00$ and $Re = 100$, where $\alpha \in [0, 2\pi]$ is the forcing phase. For other forcing parameters we obtain the same qualitative features than what we describe for Figure 8. We observe that a “corona”-like region appears around the cylinder with negative values of ϕ . Figure 8(a) shows the phase when ϕ is the most negative, where we can expect the strongest possible centrifugal instability with the highest growth rate (Bayly (1988)). The location \bar{x}_{\max} , where the instability can be the most strong locally, is given by $|\phi(\bar{x}_{\max})| = |\phi_{\max}|$.

Figure 8(b) and 8(c) describe the evolution of $\phi(\bar{x}, \alpha)$ for forcing phases that correspond to the mean and the minimum values, where the flow is less receptive to the instability. We observe that $\phi(\bar{x}, t)$ is x -symmetric regarding the forcing phase, $\phi(x, y, \alpha) = \phi(x, -y, \alpha + \pi)$. In Figure 9 we show the variation of the lift coefficient $c_L = L/\frac{1}{2}\rho U_\infty^2$, being L the resulting lift force,

¹It should be noted that viscous effects have to be considered to determine the actual stability criterion. This could be done using d_c in the definition of the Taylor number T of equation 1.

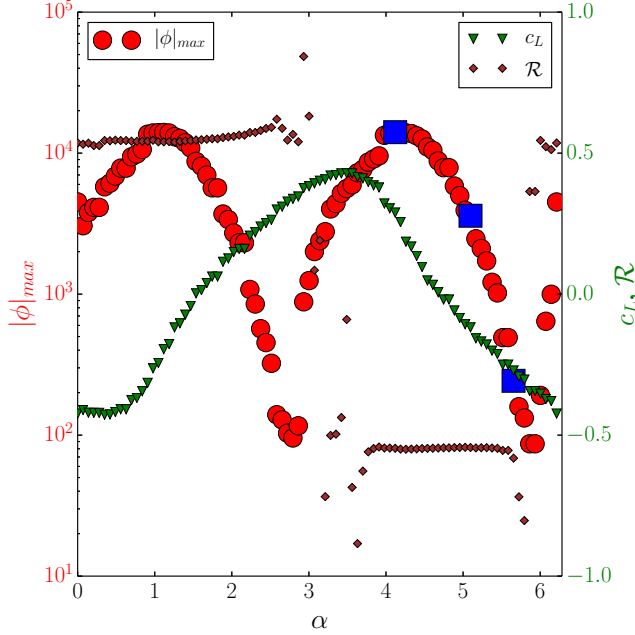


Figure 9: $|\phi|_{\max}$, red circle symbols, is the maximum of the Rayleigh discriminant modulus in function of the forcing phase α , $|\phi|_{\max} = |\phi(\bar{x}_{\max}, \alpha)|$. The lift coefficient c_L , green triangle symbols, gives a reference for the forcing phase α . The local radius of curvature value \mathcal{R} , brown diamond symbols, at \bar{x}_{\max} is close to the cylinder radius, its sign changes with the shedding cycle. Blue square symbols \blacksquare mark three forcing phases depicted in Fig. 8.

which is correlated with the phase reference α . The local radius \mathcal{R} calculated from Eq. (6) in \bar{x}_{\max} is also represented, we can see that its modulus is close to the value of the cylinder radius as the curved streamlines of the forced flow approach the cylinder. The sign of the local radius accompanies the changes due to the oscillation. We present in the same Figure a curve for the evolution of the maximum of the Rayleigh discriminant modulus $|\phi(\bar{x}, t)|_{\max}$ during a forcing period. We indicate over this curve the three values of $|\phi|_{\max}$ that lead to the construction of Figure 8.

As we have already pointed out, we can extract a convenient length scale in order to adapt our problem to the pure centrifugal instability framework, allowing us to compare our results with previous works. If we consider the forcing phase that corresponds to $|\phi|_{\max}$, around $\alpha = 4$ in Figure 9, the 2D flow streamlines are depicted by Figure 10(a). Using equation 1, the Rayleigh discriminant is obtained and presented in Figure 10(b). It is worth mentioning that a y -symmetric field is retrieved for $\alpha \simeq 1$ that corresponds to the other maximum of $|\phi|$. Image processing is used in order to extract a length scale from a contour plot of the Rayleigh discriminant obtained from equation (1) as shown in Figure 10(c) (see Appendix for details). The mean radius represented in Figure 10(c) determines the length scale d_c related to the size of the unstable region for 2D flow. It is shown in Figure 11(a) for different forcing frequencies at a fixed forcing amplitude $A = 4.00$ together with the size $\lambda_z/2$ of the centrifugal rolls that develops in the 3D flow. Both d_c and $\lambda_z/2$ follow the same $(f^+)^{-1/2}$ trend, supporting the idea of the pulsed Stokes layer. Their ratio, around a value of 3, is plotted in Figure 11(b). Given

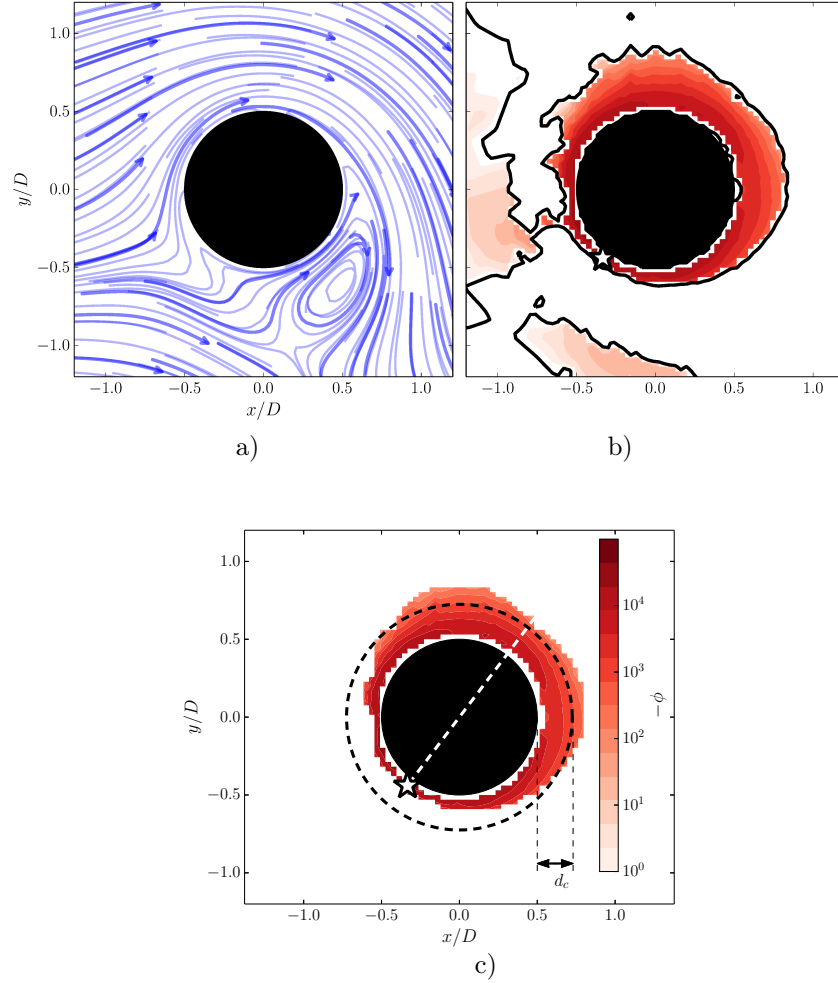


Figure 10: For $(f^+ = 0.75, A = 4.00)$ at the forcing phase α_{max} corresponding to $\phi_{max} = \phi(\bar{x}, \alpha_{max})$: a) Streamlines. b) Regions of negative Rayleigh discriminant $-\phi$. The spatial minimum of ϕ is placed at a position identified with the symbol \star . c) ϕ regions after image processing. The corresponding mean radius for ϕ is represented and the resulting measure d_c is indicated.

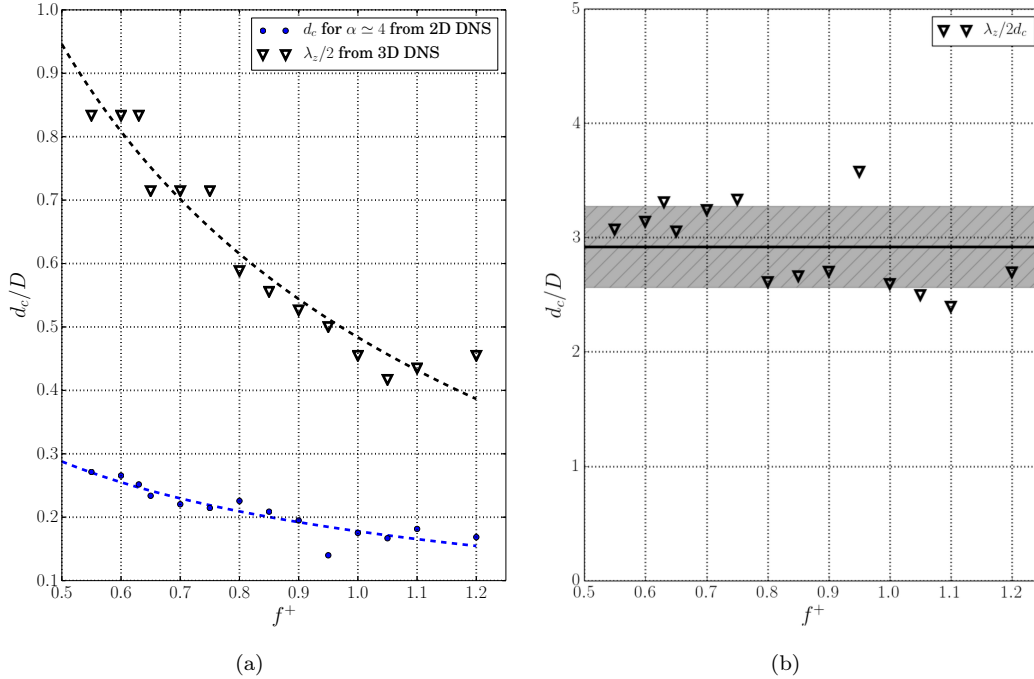


Figure 11: For a fixed forcing amplitude $A = 4.00$, variation of the estimated centrifugal instability measure d_c at $\alpha \simeq 4$ from 2D DNS and variation of the wavelength λ_z associated with the size of the rolls in Figure 5(a). b) Ratio between the characteristic length d_c for the centrifugal instability determined from 2D simulations and $\lambda_z/2$ issued from 3D simulations. The thick black line represents the mean value of $\lambda_z/2$.

that the flow is under non-stationary forcing, the rolls are formed periodically symmetric with respect to the x -axis. Besides, d_c has been determined for a particular phase $\alpha \simeq 4$, where the instability is most intense, but the centrifugal instability region changes its size. These arguments may explain the difficulty for estimating d_c and the scale difference between $\lambda_z/2$ and d_c . Nevertheless, we can observe that the main behaviour is shared between λ_z and d_c , therefore, a centrifugal instability region observed in 2D simulations is in agreement with the 3D instability that develops in 3D DNS.

5 Conclusions

The present work gives a new view about 3D instabilities in wake flows. In the context of forced wakes at moderate Reynolds numbers, we found a new transition that leads to the formation of three dimensional structures. The instability shares aspects that were previously studied for centrifugal pulsed flows. Taylor Couette-like vortices develop from a definite threshold of forcing parameters (f, A) and these structures are modified by the incoming flow. For this complex instability, 2D evaluation of the Rayleigh discriminant ϕ may give a fast criterion to determine whether a wake flow becomes three dimensional or not. We found from streamline shapes and the spatial distribution of ϕ that the problem shares some analogy in relation to

eccentric Taylor Couette flows.

As 2D forcing in wakes may indeed trigger 3D structures, this behaviour must be taken into account in flow control schemes. Streamlines which result too much “bent“ by forcing in wakes can make evident strong negative values of the Rayleigh discriminant ϕ and thus the possibility of a centrifugal instability.

On the other hand, this simple problem can offer an interesting benchmark to study instabilities and transition to turbulence from oscillatory rotation.

6 Appendix: Determination of the centrifugal instability region length.

The choice of a characteristic length of the centrifugal instability region from the Rayleigh discriminant scalar fields is not straightforward as we observe Fig. 8. we choose to select the forcing phase that corresponds to the minimum value of ϕ , the most unstable state. Figure 10(b) presents such state but the ϕ scalar field needs to be more clear in order to extract a length d_c . Simple image processing functions, erosion and dilation, are applied successively to the scalar field in order to obtain Fig 10(c), where a clear shape is noticed. We found that such shape has an aspect that resembles an eccentric cylinder gap. Therefore, we choose as a characteristic length the mean radius of this gap $d_c = 1/(2\pi) \int_0^{2\pi} r d\varphi - D/2$, with r the shape radius varying with the angular coordinate φ .

6.1 Convergence analysis for DNS

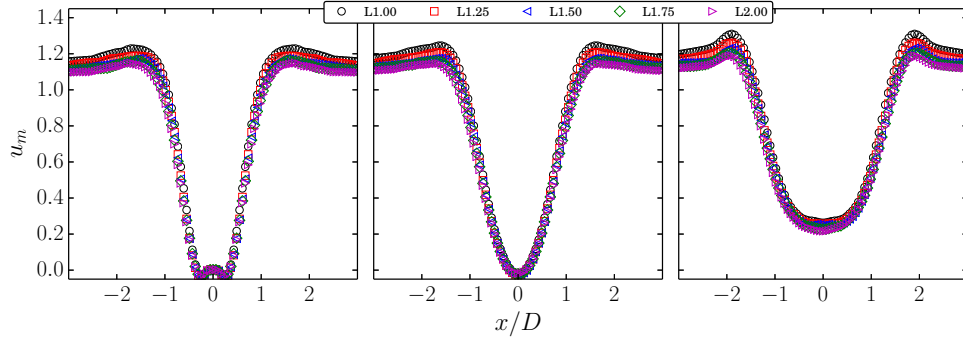
In order to ensure that the results do not depend on the size of the domain we chose, we performed a convergence analysis for the 2D case. Given that the domain size of the reference study is $L_x \times L_y = 20D \times 10D$, we label it as $L1.00$. As we selected larger domains which scale as $[1.25; 1.50; 1.75; 2.00]$ the reference study length, we label them $L1.25$, $L1.50$, $L1.75$ and $L2.00$. For these scaling lengths, we plotted mean flow profiles for the streamwise component of the velocity u_m at three different x positions $x = 0.5D$, D , $2D$ in Fig. 12(a). Figure 12(b) presents for the same direction, fluctuations intensity u_{rms} profiles for the same different x positions. We observe that changing the domain size does not modify the flow dynamics. Lift coefficient is also calculated for each case as it is presented in Fig.13. We also observe good agreement between the different scaling domains.

Data Accessibility

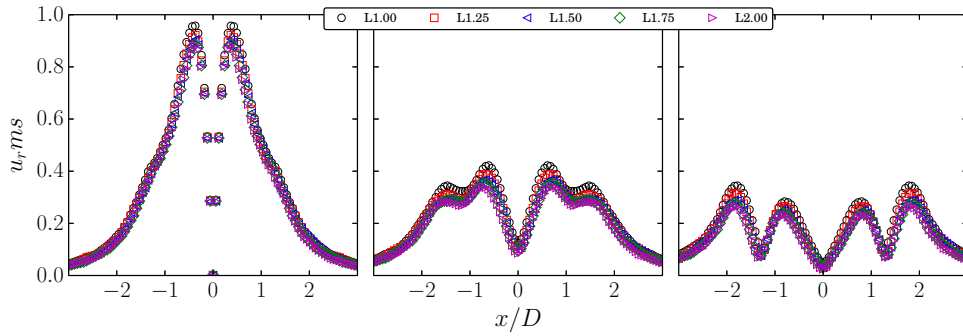
In order to reproduce all the calculations included in this paper, Gerris(Popinet, 2003) is available free of charge under the Free Software GPL license and our code files can be downloaded from this URL.

Acknowledgment

We acknowledge support from the LIA PMF-FMF (Franco-Argentinian International Associated Laboratory in the Physics and Mechanics of Fluids), Argentina - France.



(a)



(b)

Figure 12: For the forcing case $f^+ = 1.00$ and $A = 3.50$ we test the reference scale $L1.00$ versus larger scales up to $L2.00$. (a) Mean flow profiles u_m at $x = 0.5D$, $x = D$ and $x = 2D$ for the different scales tested. (b) Fluctuations intensity u_{rms} for flow profiles at the same locations.

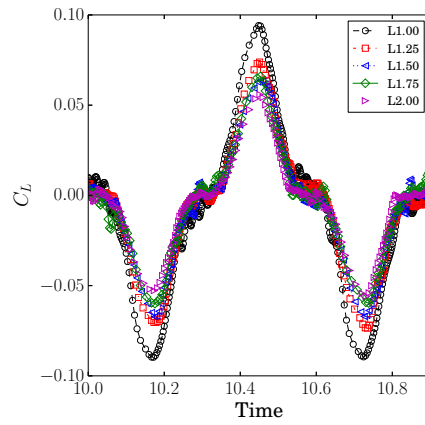


Figure 13: For the forcing case $f^+ = 1.00$ and $A = 3.50$, the lift coefficient C_L evolution during two forcing periods corresponding to five different scale domains.

References

- A Aouïdef, C Normand, A Stegner, and J E Wesfreid. Centrifugal instability of pulsed flow. *Physics of Fluids*, 6(11):3665–3676, 1994.
- B J Bayly. Three dimensional centrifugal type instabilities in inviscid two dimensional flows. *Physics of Fluids*, 31:56–64, 1988.
- J. F. Beaudoin, O. Cadot, J. L. Aider, and J E Wesfreid. Three-dimensional stationary flow over a backward-facing step. *European Journal of Mechanics B-Fluids*, 1:147–155, 2004.
- H. Bénard. Formation périodique de centres de giration à l’arrière d’un obstacle en mouvement. *C. R. Acad. Sci.*, 147:839–842, 1908.
- H Blackburn, F Marques, and J M Lopez. Symmetry breaking of two-dimensional time-periodic wakes. *Journal of Fluid Mechanics*, 522:392–411, 2005.
- S Carmi and J I Tustaniwskyj. Stability of modulated finite-gap cylindrical couette flow: linear theory. *Journal of Fluid Mechanics*, 108:19–42, 1981.
- S Chandrasekhar. *Hydrodynamic and hydromagnetic stability*. Dover Publications, 1981.
- J D’Adamo, R Godoy-Diana, and J E Wesfreid. Spatio-temporal spectral analysis of a forced cylinder wake. *Physical Review E*, 84(5):1–8, 2011.
- P G Drazin and W H Reid. *Hydrodynamic stability*. Cambridge University Press, 1981.
- J R Elston, Sheridan J, and H Blackburn. Two-dimensional floquet stability analysis of the flow produced by an oscillating circular cylinder in quiescent fluid. *European Journal of Mechanics B-Fluids*, 23:99–106, 2004.
- P Ern. A study on time-periodic finite-gap taylor-couette flows. *C. R. Acad. Sci. Paris, Ser. Iib: Mec., Phys., Chim., Astron.*, 326:727–732, 1998.
- P Ern and J E Wesfreid. Flow between time-periodically co-rotating cylinders. *Journal of Fluid Mechanics*, 397:73–98, 1999.
- P Ern and J E Wesfreid. Time behavior of the secondary flow between time-periodically corotating cylinders: A two-frequency forcing case. *Physical Review E*, 65:1–4, 2002.
- P Hall. The stability of unsteady cylinder flows. *Journal of Fluid Mechanics*, 67:29–63, 1975.
- P Hall. On the stability of the unsteady boundary layer on a cylinder oscillating transversely in a viscous fluid. *Journal of Fluid Mechanics*, 146:347–367, 1984.
- H Honji. Streaked flow around an oscillating circular cylinder. *Journal of Fluid Mechanics*, 107: 609–620, 1981.
- C. P. Jackson. A finite-element study of the onset of vortex shedding in flow past variously shaped bodies. *Journal of Fluid Mechanics.*, 182:23–45, 1987.
- S Kumar, C Lopez, O probst, G Francisco, D Askari, and Y Yang. Flow past a rotationally oscillating cylinder. *Journal of Fluid Mechanics*, 735:305–346, 2013.
- S Leblanc and C Cambon. Effects of the coriolis force on the stability of stuart vortices. *Journal of Fluid Mechanics*, 356:353–379, 1998.

- C Leclercq, B Pier, and J F Scott. Temporal stability of eccentric taylor-couette-poiseuille flow. *Journal of Fluid Mechanics*, 733:68–99, 2013.
- D Lo Jacono, J Leontini, M Thompson, and Sheridan J. Modification of three-dimensional transition in the wake of a rotationally oscillating cylinder. *Journal of Fluid Mechanics*, 643: 349–362, 2010.
- S Popinet. Gerris: a tree-based adaptive solver for the incompressible euler equations in complex geometries. *Journal of Computational Physics*, 190(2):572 – 600, 2003.
- J O Pralits, F Giannetti, and L Brandt. Three-dimensional instability of the flow around a rotating circular cylinder. *Journal of Fluid Mechanics*, 730:5–18, 2013.
- M. Provansal, C. Mathis, and L. Boyer. Bénard-von Kármán instability: transient and forced regimes. *Journal of Fluid Mechanics.*, 182(-1):1–22, 1987.
- J W S Rayleigh. On the dynamics of revolving fluids. *Proceedings of the Royal Society of London. Series A, Mathematical and Physical Sciences*, 93:148–154, 1916.
- P J Riley and R L Laurence. Linear stability of modulated circular couette flow. *Journal of Fluid Mechanics*, 75:625–646, 1976.
- W Saric. Görtler vortices. *Annual Review of Fluid Mechanics*, 26:379–409, 1994.
- G Seminara and P Hall. Centrifugal instability of a stokes layer: Linear theory. *Proceedings of the Royal Society of London. Series A, Mathematical and Physical Sciences*, 350:299–316, 1976.
- C Shu, L Wang, Y T Chew, and N Zhao. Numerical study of eccentric couette-taylor flows and effect of eccentricity on flow patterns. *Theoretical and Computational Fluid Dynamics*, 18: 43–59, 2004.
- L Shoa Siong. An experimental investigation of taylor couette flow between eccentric cylinders. Master’s thesis, National University of Singapore, 2006.
- D Sipp and L Jacquin. A criterion of centrifugal instabilities in rotating systems. In Agnès Maurel and Philippe Petitjeans, editors, *Vortex Structure and Dynamics*, volume 555 of *Lecture Notes in Physics*, pages 299–308. Springer Berlin Heidelberg, 2000.
- S. Taneda. Visual observations of flow past a circular-cylinder performing a rotatory oscillation. *Journal of the Physical Society of Japan*, 45(3):1038–1043, 1978. ISSN 0031-9015.
- M Tatsuno and P W Bearman. A visual study of the flow around an oscillating circular cylinder at low keulegan-carpenter numbers and low stokes numbers. *Journal of Fluid Mechanics*, 211: 157.182, 1990.
- B. Thiria and J. E. Wesfreid. Stability properties of forced wakes. *Journal of Fluid Mechanics.*, 579:137–161, 2007.
- B. Thiria, S. Goujon-Durand, and J. E. Wesfreid. Wake of a cylinder performing rotary oscillations. *Journal of Fluid Mechanics.*, 560:123–147, 2006.
- T. von Kármán. Über den mechanismus des widerstandes, den ein bewegter körper in einer flüssigkeit erfährt. *Nachr. Ges. Wissenschaft. Göttingen*, pages 509–517, 1911.